journal of the mechanical behavior of biomedical materials 153 (2024) 106505

Contents lists available at ScienceDirect

Journal of the Mechanical Behavior of Biomedical Materials

journal homepage: www.elsevier.com/locate/jmbbm

Research paper

Anisotropic plates with architected tendon network

Md Shahjahan Hossain, Hossein Ebrahimi, Ranajay Ghosh *

Department of Mechanical and Aerospace Engineering, University of Central Florida, Orlando, FL, United States of America

ARTICLE INFO

Keywords:
Metamaterials
Anisotropy
Bending rigidity
Finite element (FE) modeling

ABSTRACT

We synthesize geometrically tailorable anisotropic plates by combining button shaped fish-scale like features on soft substrates, then lacing them with high-stiffness strings. This creates a new type of biomimetic architectured structure with multiple broken symmetries. First, the tendons and substrate together break the symmetry of the bending response between the concave and convex curvature. Next, the weave pattern of the tendons further breaks symmetry along the two directors of plates. The anisotropy is clearly evident in 3-point bending experiments. Motivated by these experiments and the need for design, we formulate an analytical energy-based model to quantify the anisotropic elasticity. The derived architecture-property relationships can be used to design architected tendon plates with desirable properties.

1. Introduction

Slender unremarkable substrates can be transformed into materials with extraordinary mechanical properties with an additional metastructure on one side. This has recently been exploited in biomimetic fish scale-inspired designs (Tatari et al., 2023; Ebrahimi et al., 2021; Buehler, 2006; Wegst et al., 2015; Helfman et al., 2009; Ghosh et al., 2014; Hossain et al., 2022), membrane tensegrity (Skelton et al., 2001; Lu and Skelton, 1998; Zhang and Ohsaki, 2015) and metasurfaces (Munyensanga and El Mabrouk, 2023; He et al., 2018; Arbabi et al., 2017; Badawe et al., 2016; Martini and Maci, 2014; Wu et al., 2019; Lu et al., 2022; Yu et al., 2018). Adapting them for active structures requires complex integration of stimuli-responsive materials or fluidic circuits, leading to additional complexity.

Tendons, Fig. 1(a) are string like structures whose intricate arrangements are often exploited in nature to transfer force from muscles to bones and adapted for robotic operation due to their lightweight, tailorability and silent operation (Rutherford et al., 2015; Usman et al., 2017; Souza et al., 2019; Jang et al., 2022; Popov et al., 2013). Thus woven (Stig and Hallström, 2013) and tendon designs (Jeong et al., 2021) remains one of the most exciting areas in modern soft and wearable applications as shown in Fig. 1(b). With the advent of new types of fibers (Bundhoo et al., 2009), periodic tendon networks can create novel metastructures capable of tailorable mechanical properties. The strings/tendons themselves could be replaced by actuators such as coiled actuators (Zhang et al., 2020; Souza et al., 2019), thermal actuators (Rodrigue et al., 2017; Knick et al., 2019; Jing et al., 2016), and humidity actuators (Wang et al., 2018; Pu et al., 2022). Although bearing resemblance to membrane tensegrity, tendon structures considered here are soft plates adorned with strings that are not inherently under tension.

The architecture of the periodic network or weave of the tendons can be exploited to create desirable mechanical stiffness when integrated with a substrate. Such designs lead to metastructures with unique and tailorable mechanical properties not seen in conventional designs. For instance Fig. 1(c)–(d) shows tendon network structures with strings wound around pillar like buttons embedded into a soft substrate. For this type of structure, string side (convex) bending adds stiffness from tension, while the opposite side (concave bending) resembles substrate behavior until the buttons engage or become jammed, resulting in a tailorable bi-directional metastructure. Despite potential applications to smart materials, little is known about their elasticity or architecture-property relationship required for design. This lack of architecture-property relationships hinders further design-driven growth and exploration. We address this gap for the first time by systematic derivation of closed form relationships using energy principles (Mousanezhad et al., 2016; Yu et al., 2018).

2. Motivating experiments

To create a motivating sample, we make a mold with dimension 212 mm $(Length) \times 65$ mm $(Width) \times 10$ mm $(Height)$ using a 3D (Ultimaker™) printer. Separately, we used Formlabs 3D printer to fabricate buttons (Polylactic acid, PLA) ($E_{PLA} \sim 3$ GPa) We poured mixtures of silicone rubber (Vinylpolysiloxane (VPS)) (~1.5 MPa) (Ebrahimi, 2021) and curing material (1:1) into the mold. After curing, buttons were

* Corresponding author.
E-mail address: ranajay.ghosh@ucf.edu (R. Ghosh).

https://doi.org/10.1016/j.jmbbm.2024.106505
Received 4 December 2023; Received in revised form 23 February 2024; Accepted 11 March 2024
Available online 15 March 2024

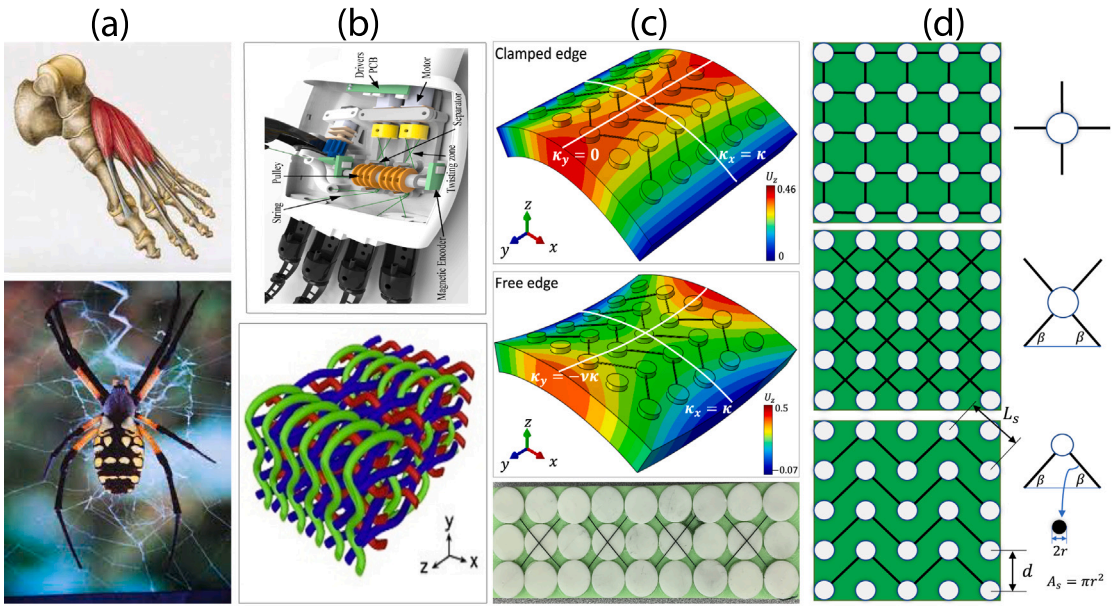

Fig. 1. String/tendon structures, (a) in nature: toe joints (tendon-bone structure) (top) and spider fiber (the golden orb weaver) (bottom) (Skelton and De Oliveira, 2009) (b) bionic hand (top) (Tavakoli et al., 2015) and 3D woven composite structure (bottom) (Stig and Hallström, 2013) (c) implemented in this study: (top and middle) to develop mathematical model and carry out the simulation, (bottom) an illustration of a string-substrate system employed in an experimental setup (d) configurations of string and its geometry.

pushed into the soft substrate without adhesives. String (Power Pro Spectra Fiber Braided Line) ($dia \sim 0.35$ mm) were wound once around the button in four different arrangements to complete the fabrication.

To demonstrate weave effect, we performed 3-point bending experiments using MTS Insight® under displacement control at a cross-head speed of 1 mm/s with cross-head displacement from 0 – 50 mm. Here, we tested eight distinct samples with buttons placed next to each other with minimal gaps. These samples included: without string (S_0), one zigzag string (Z_1) at 45° angle, two zigzag strings (Z_2) at 45° angle, and two straight strings at 0° angle, as shown in Fig. 1. We used string side loading (convex) and button side loading (concave) for obtaining the stiffness.

The load–displacement curves, Fig. 2, show that convex stiffness is significantly higher for Z_2 and then decreases in the order of Z_1 and S_2 when compared to baseline (no string). Conversely, the behavior on the concave side is unfettered by the strings as they are not engaged. Eventually, the structure reaches a geometrically dictated locking/jamming configuration when the buttons touch each other. The potential application for this system lies in tailorable structures and soft robotics. One of the features of this system remains the use of weave architecture to create programmable stiffness. Hence, under same loads, deflections can be changed by simply changing the wrap up of the strings around the pillars. We use two different weaves to show the change in deflection of a cantilevered plate under its own self weight, Fig. 3. The effectiveness of this strategy becomes clear when we note that significant difference in deflection occurs with just three rows of buttons. These results inspire us to develop a mathematical architecture-property relationship for the string-substrate systems.

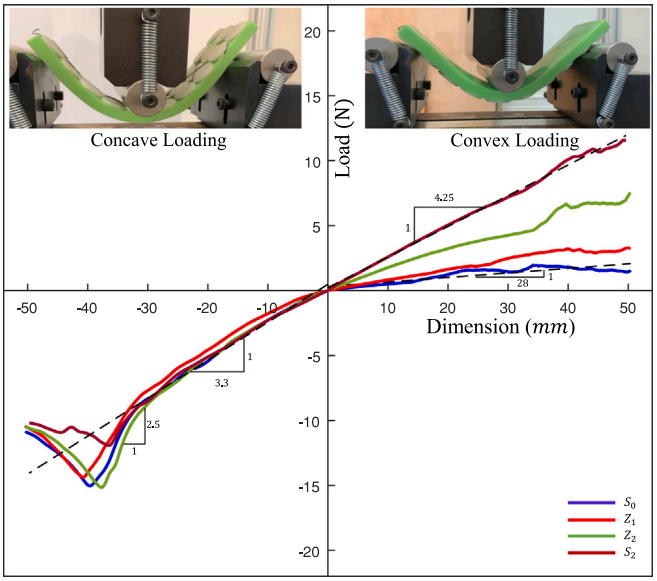

Fig. 2. Load vs displacement curve for 3 point bending (edit).

3. Analytical model development

Our mathematical model considers a single type of unit cell, that of Z_1 type as its parameters can encompass all the other unit cells considered in this work, Fig. 1(d).

We take E_b and E_s as the modulus of elasticity of substrate (base) and string respectively leading to modulus ratio $\mu = \frac{E_s}{E_b}$. From the geometry of the unit cell as shown in Fig. 4, we denote the length of the string from center to center of the button, button radius, the thickness of the substrate, and the cross-sectional area of the string as L_s, R, h and A_s respectively. Although, actual string length into the unit cell would be $L_{s0} = L_s - 2R$, for our theoretical development, we take $R \ll L_{s0}$ and hence $L_{s0} \approx L_s$. Furthermore, we consider the angle of the string in a unit cell with respect to x-direction as β, the height of the protruding button as H, and button embedded length as H_e, Fig. 4. For brevity we use $\cos\beta \equiv C_\beta$ and $\sin\beta \equiv S_\beta$.

We consider two canonical deformation boundary conditions (BC) to measure effective rigidity - (1) opposite pair of clamped edges (i.e. for longitudinal curvature as $\kappa_x = \kappa$ and transverse curvature as $\kappa_y = 0$), and (2) opposite pair of free edges (i.e. for longitudinal curvature as $\kappa_x = \kappa$ and transverse curvature as $\kappa_y = -\nu\kappa$). We also consider two different high-contrast material regimes. In one case — much stiffer strings than the substrate and in the other (high-μ), much stiffer substrate compared to strings (low-μ). These two extreme cases help envelope the design space of tendon structures. We assume that the buttons are perfectly bonded to the substrate and strings do not slip

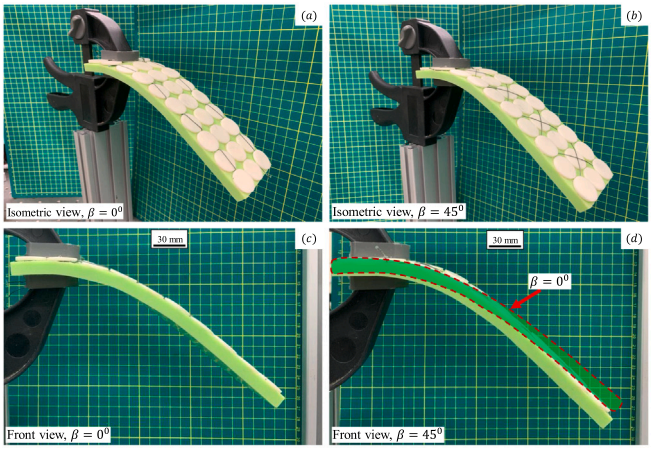

Fig. 3. Practical demonstration of uses of string architecture alone in tailoring response against same load (here self weight).(a) and (b) depict the isometric view of the samples for $\beta = 0°$ and $\beta = 45°$, respectively. (c) and (d) display the front view for both samples.

till very large deformations. Although the overall deformation of the structure is a combination of rotation of the buttons and the extension of the strings, the kinematics differ between material properties regimes (μ values).

3.1. High μ regime

In the high $\mu(\sim\mathcal{O}(10^3))$ regime, we assume negligible string extension (rigid body constraint). For that, we considered two distinct kinematic conditions. In one scenario, the buttons within a unit cell rotate about their bases during convex bending to uphold inextensibility, while in another scenario, the button tips return to their reference configuration to preserve inextensibility. These are illustrated in SM-1,2. Imposing periodicity, for the first model, we find that two adjacent string segments move in equal and opposing directions (See SM-1). If imposed principal convex curvatures are κ_x, κ_y, the opposing button motion leads to button rotation (tilt), $\theta(\kappa_x, \kappa_y) = \frac{L_s}{4H} h \frac{\kappa_x C_\beta^2 + \kappa_y S_\beta^2}{(1+\kappa_2 h/2) S_\beta}$ and $\theta \approx \frac{L_s}{4H} h(\kappa_x C_\beta^2 + \kappa_y S_\beta^2)$ for theory-1 and theory-2 respectively (See SM-1,2). The total elastic energy areal density (per unit plate area) is $u = u_P + \frac{1}{2}\sigma K_B \theta^2$, where u_P is the areal energy density of the plate-like substrate, K_B is base rotational stiffness of the buttons as they rotate on the substrate (assuming linear rotational springs) and $\sigma = N_s/L_b^2$, N_s as the number of unit cells (half number of buttons to prevent counting twice), σ is areal unit cell density. Prior work (Ghosh et al., 2014; Ebrahimi, 2021) has shown that $K_B \sim \upsilon_{in} E_b$, where υ_{in} is a volume factor that reflects the embedded button geometry. For the clamped edge case, $u_P = \frac{1}{2} C_f D_0 \kappa^2$, and for free edge case, $u_P = \frac{1}{2} C_f D_0 (1-\nu^2)\kappa^2$ with imposed curvature of κ, bending rigidity (Timoshenko et al., 1959), $D_0 = \frac{1}{12}\frac{E_b h^3}{1-\nu^2}$, C_f is non-dimensional button inclusion factor that measures the effect of button embedding into the substrate leading to inclusion effect. These energy expressions can be used to compute effective plate bending rigidity in either direction using, $D_i = \partial^2 u/\partial \kappa_i^2$. Here, D_i are computed by giving κ_i while the other direction conforms to the overall BC. Using $\bar{D}_i = D_i/D_0$, we get the normalized anisotropic bending rigidities for the high-μ regime shown in Table 1. Here, ϕ_{in} is total button embedded volume fraction and $\eta = H/L_s$ is height ratio.

3.2. Low μ regime

When strings are softer, ($\mu \sim \mathcal{O}(10)$), additional strains come from string stretching (See SM-2). We assume that the total strain in the string can be additively decomposed into two parts — first is a conformal string strain (ϵ_{conf}) that arises when buttons rotate following the Kirchoff bending kinematics without additional relative rotation with respect to substrate. After this deformation, the string undergoes a 'correction' due to the rotation of the buttons from the ensuing string tension of the previous step. This 'correction strain' ϵ_{corr}, together with ϵ_{conf} is the total string strain, $\epsilon_s = \epsilon_{conf} + \epsilon_{corr}$ (see SM-2). The total elastic energy density can be expressed as, $u = u_P + \frac{1}{2}\phi_v E_s \epsilon_s^2 h + \frac{1}{2}\sigma K_B \theta^2$, where $\phi_v = \frac{2N_s A_s L_s}{L_b^2 h}$ is the volume fraction of the fibers. Note that $\frac{1}{2} E_s \epsilon_s^2 h$ is essentially the elastic energy volume density of the tendons integrated over the plate thickness, typical in plate theory formulations. As mentioned earlier, using these energy expressions we obtain the following normalized anisotropic bending rigidities for clamped and free boundary cases for both direction, as shown in Table 1. Here, ϕ_v is volume fraction of string and $p = \frac{2H}{h}$ is protrusion ratio (see SM-2). Similarly, in the free edge case, we get the non-dimensional bending rigidities in both directions as shown in Table 1 (see SM-2).

4. Numerical study

We use commercial FE software ABAQUS/CAE 2021 (Dassault Systémes) for validation. The digital models conformed to the analytical model. To simplify the model, we have included a total of 25 buttons in our finite element modeling. Ideally, the analytical model is applicable where there are large numbers of unit cells. However, it is well known that for small strain gradients, lack of localized loads or small strains, relatively few unit cells can provide a reasonably good approximation (Ebrahimi et al., 2020). Due to this factor, there would be some inaccuracies in absolute values between our analytical model and full scale structural simulation. However for similar systems such a fish scale, even these non-ideal effects were not found to deter from the overall trends or physics of the problem (Ali et al., 2019). The buttons were subjected to rigid body constraints, eliminating the need for button material attributes. Substrate modulus (E_b) were taken to be 0.166 MPa (same as Dragon Skin material). Poisson ratio (ν) of 0.48 was used to model nearly incompressible nature of the polymeric substrate (Lim et al., 2020; Amendola et al., 2014). String modulus (E_s) were taken to be either 5480 MPa or 9 MPa to cover the High-μ and low-μ ranges. The string's Poisson's ratio were taken as 0.25. Eight unit cells represented the tendon system. Non-linearity was negligible for this small strain study and the rotation was applied at the ends of the plate to impose the curvature. We used mesh size as 0.8 (standard quadratic 3D stress elements-C3D10) and found sufficient for mesh convergence. Using FE and K_B scaling law introduced earlier, we obtain $K_B = 4.72E_b + 0.64$ for buttons with exposed height $H = 0.7$ mm, embedded height $H_e = 5.9$ mm, and button radius at the top $R = 2.5$ mm (See SM-3). We implemented curvature by applying rotational boundary conditions to the structure, while ensuring the required constraint on the curvature for the opposite side. To apply the load to a specific edge, we initially established reference points on each edge and established coupling between the reference point and the corresponding surface on that side. When applying clamped edge boundary conditions, we utilized continuum distribution in the transverse edge coupling and kinematic distribution in the longitudinal direction coupling. For free edge boundary conditions, we applied continuum distribution constraints to both longitudinal and transverse direction couplings. Through simulations, we obtained the curvature and its corresponding all strain energy and moment values as per the requirement. The bending rigidity of the structure was then calculated using gradient of these data. Similarly we calculate, C_f to be either 1.1 or 1.25 depending on BC (See SM-3). We also postulate that the Poisson ratio of the substrate and the overall composite tendon structure are nearly same. Our simulations show this to be a good approximation (See SM-4). Finally, note that the two sets of formulas for different μ ranges do not overlap due to different kinematic assumptions. Also note that for structurally macroscopic systems for such structure, true periodicity is difficult to achieve. However in the absence of high strain

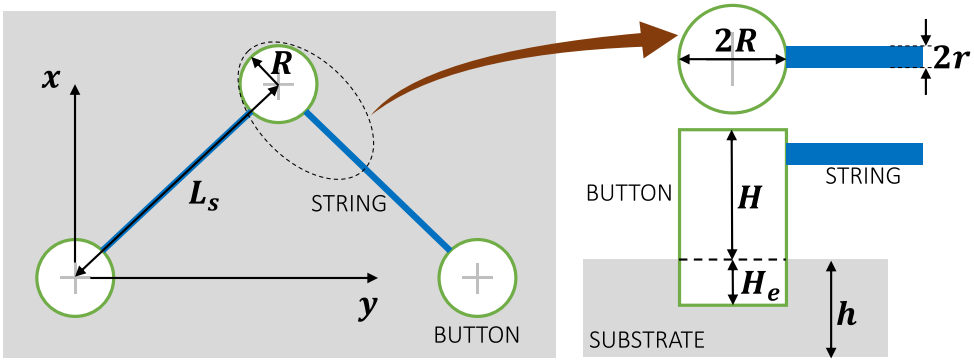

Fig. 4. Unit cell illustrations — top view (left) and partial top view (top right) and partial side view with substrate relative position of individual buttons (right bottom) (edit).

Table 1
Bending rigidity expressions.

μ-regimes	BC	D_x	D_y
High	Clamped	Theory 1: $\bar{D}_x^{clmp} = C_f + \frac{3}{4}\frac{\phi_{in}}{\eta^2}(1-\nu^2)\frac{C_\beta^4}{S_\beta^2}$	Theory 1: $\bar{D}_y^{clmp} = C_f + \frac{3}{4}\frac{\phi_{in}}{\eta^2}(1-\nu^2)S_\beta^2$
High	Clamped	Theory 2: $\bar{D}_x^{clmp} = C_f + \frac{3}{4}\frac{\phi_{in}}{\eta^2}(1-\nu^2)C_\beta^4$	Theory 2: $\bar{D}_x^{clmp} = C_f + \frac{3}{4}\frac{\phi_{in}}{\eta^2}(1-\nu^2)S_\beta^4$
High	Free	Theory 1: $\bar{D}_x^{free} = C_f(1-\nu^2) + \frac{3}{4}\frac{\phi_{in}}{\eta^2}(1-\nu^2)\frac{(C_\beta^2-\nu S_\beta^2)^2}{S_\beta^2}$	Theory 1: $\bar{D}_y^{free} = C_f(1-\nu^2) + \frac{3}{4}\frac{\phi_{in}}{\eta^2}(1-\nu^2)\frac{(S_\beta^2-\nu C_\beta^2)^2}{S_\beta^2}$
High	Free	Theory 2: $\bar{D}_x^{free} = C_f(1-\nu^2) + \frac{3}{4}\frac{\phi_{in}}{\eta^2}(1-\nu^2)(C_\beta^4 + \nu^2 S_\beta^4 - 2\nu C_\beta^2 S_\beta^2)$	Theory 2: $\bar{D}_y^{free} = C_f(1-\nu^2) + \frac{3}{4}\frac{\phi_{in}}{\eta^2}(1-\nu^2)(S_\beta^4 + \nu^2 C_\beta^4 - 2\nu C_\beta^2 S_\beta^2)$
Low	Clamped	$\bar{D}_x^{clmp} = C_f + 3\phi_v\mu(1-\nu^2)(1+p)^2C_\beta^2(1-\frac{S_\beta^2}{\Gamma})^2 + \frac{3}{\eta^2}(1+p)^2\phi_{in}(1-\nu^2)(\frac{C_\beta S_\beta}{\Gamma})^2$	$\bar{D}_y^{clmp} = C_f + 3\phi_v\mu(1-\nu^2)(1+p)^2S_\beta^2(1-\frac{S_\beta^2}{\Gamma})^2 + \frac{3}{\eta^2}(1+p)^2\phi_{in}(1-\nu^2)(\frac{S_\beta^2}{\Gamma})^2$
Low	Free	$\bar{D}_x^{free} = (1-\nu^2)[C_f + 3\phi_v\mu(1+p)^2B_a^2(1-\frac{S_\beta^2}{\Gamma})^2 + \frac{3}{\eta^2}(1+p)^2\phi_{in}(\frac{B_aS_\beta}{\Gamma})^2]$	$\bar{D}_y^{free} = (1-\nu^2)[C_f + 3\phi_v\mu(1+p)^2B_b^2(1-\frac{S_\beta^2}{\Gamma})^2 + \frac{3}{\eta^2}(1+p)^2\phi_{in}(\frac{B_bS_\beta}{\Gamma})^2]$
High μ	Theory 1: $\bar{D}_{xy} = \nu C_f + \frac{3}{8}\frac{\phi_{in}}{\eta^2}(1-\nu^2)(S_\beta^2 - C_\beta^2\kappa_x h - \frac{1}{2}S_\beta^2\kappa_y h)$, Theory 2: $\bar{D}_{xy} = \nu C_f + \frac{3}{4}\frac{\phi_{in}}{\eta^2}(1-\nu^2)S_\beta^2C_\beta^2$		
Low μ	$\bar{D}_{xy} = \nu C_f$		
Parameters	$\phi_{in} = 2N_s v_{in}/L_b^2 h$, $\phi_v = \frac{2N_s A_s L_\perp}{L_b^2 h}$, $\Gamma = \frac{\phi_{in}}{\phi_v}\frac{1}{\eta^2\mu} + S_\beta^2$, $B_a = \sqrt{C_\beta^2 + \nu^2 S_\beta^2}$, and $B_b = \sqrt{S_\beta^2 + \nu^2 C_\beta^2}$		

gradients, convergence is remarkably common and elastic constants exhibit good approximations for relatively smaller number of unit cells (Fish, 2003; Mousanezhad et al., 2015). We anticipate similar behavior for our case based on prior work on structurally similar fish scale systems where periodicity was relaxed but bending rigidity was found to be close to periodic assumption with similar broad trends (Ali et al., 2019). However, to allay any doubts, we carried out simulations with larger sample sizes (more unit cells) for the weave angle $\beta = 54^0$ and confirmed that changes in computed quantities such as energy density and rigidity are minor and in excellent agreement with our model. These plots are shown in SM 5.

5. Results

At high-μ, $\bar{D}$ variation with β for both BCs is shown in Fig. 5(a–b) . The FE models show excellent agreement with analytical calculations. With the increase of angle along the horizontal axis, the stiffness in the x-direction decreases, whereas the opposite is true for y-direction. At 45° weave, symmetry is restored. Stiffness change with the angle in both directions is nonlinear but with opposite rates of increase. This can be used to rapidly increase directional stiffness. Next, low-μ, $\bar{D}$ variation with β for both BCs are shown in Fig. 5(c–d). These also show an excellent match between theory and simulations. The overall anisotropy is muted for low-μ because of the lower contribution from the strings. Along with anisotropy, the nonlinearity in stiffness variation is also significantly decreased at these μ ranges. Our analytical expressions are consistent with the 3-point bending experiments. In convex bending, we observed pronounced gain in stiffness for structures with higher string volume fractions for both theory and experiment. We also compare the rigidity ratios between weaves obtained with our model. The lab tests yield a stiffness ratio of 1.75 between weaves Z_2 and Z_1, Fig. 2. Also, in this sample $\beta = 45^0$, $\nu = 0.48$, $\eta = 0.05$, $\phi_{in} = 0.0063$ for Z_1 and $\phi_{in} = 0.0125$ for Z_2. For this sample, $\mu \approx 33,000$ putting it in high-μ regime. Using these numbers and appropriate expressions, our theory predicts a bending rigidity ratio of 1.37, putting them in excellent agreement with simulations. Interestingly, for very soft strings (low-μ), $\Gamma \approx \phi_{in}/\phi_v\frac{1}{\eta^2\mu} \gg S_\beta^2$. This leads to $\bar{D}_x^{clmp} \approx C_f + 3\phi_v\mu(1-\nu^2)(1+p)^2C_\beta^2$ and $\bar{D}_y^{clmp} \approx C_f + 3\phi_v\mu(1-\nu^2)(1+p)^2S_\beta^2$. In other words, the rotational effect of button drops off. If the strings are yet too soft, i.e. ultra low $\mu(\ll 1)$ then anisotropy disappears altogether as the composite inclusion effect of the button overpowers string contribution, leading to $\bar{D}_y^{clmp} \approx \bar{D}_x^{clmp} \approx C_f$. Anisotropy is also strongly aided by high protrusion ratios p (quadratic dependence). We quantify anisotropy further by defining a normalized rigidity-divergence $\Delta\bar{D}_{xy} = |\bar{D}_x - \bar{D}_y|$. We would expect high-$\mu$ regime to be more anisotropic due to strings, but the following calculations show that geometry can be used to reverse this trend. We use only one BC case (clamped) for brevity. For the high-μ, $\Delta\bar{D}_{xy}^{clmp}|_{\mu,high} = \left|\frac{3}{4}C_{2\beta}\frac{\phi_{in}}{\eta^2}(1-\nu^2)\frac{1}{S_\beta^2}\right|$ whereas for the low-μ, $\Delta\bar{D}_{xy}^{clmp}|_{\mu,low} = \left|3C_{2\beta}(1+p)^2(1-\nu^2)\left[\left(1-\frac{S_\beta^2}{\Gamma}\right)\mu\phi_v + \frac{\phi_{in}}{\eta^2}\frac{S_\beta^2}{\Gamma}\right]\right|$. If we assume $\eta \gg 1$, i.e. very closely placed buttons, $\Gamma \sim S_\beta^2$ we get $\Delta\bar{D}_{xy}^{clmp}|_{\mu,low} \approx \Delta\bar{D}_{xy}^{clmp}|_{\mu,high} \cdot \frac{1}{4}\frac{(1+p)^2}{S_\beta^2}$. Thus if $S_\beta < \frac{1}{2}(p+1)$, we can get $\Delta\bar{D}_{xy}^{clmp}|_{\mu,low} > \Delta\bar{D}_{xy}^{clmp}|_{\mu,high}$. Hence, higher anisotropy for the softer string is only possible for relatively flat weaves and tall buttons.

Fig. 5(e) and (f) depict the stiffness $\bar{D}_{xy}$ for both analytical and finite element (FE) modeling. The bending rigidity, a cross-term involving the directions x and y shows minimal dependence on the angular variation of the string. It is evident that the bending rigidity exhibits some deviation from our theoretical predictions. This inaccuracies primarily stem

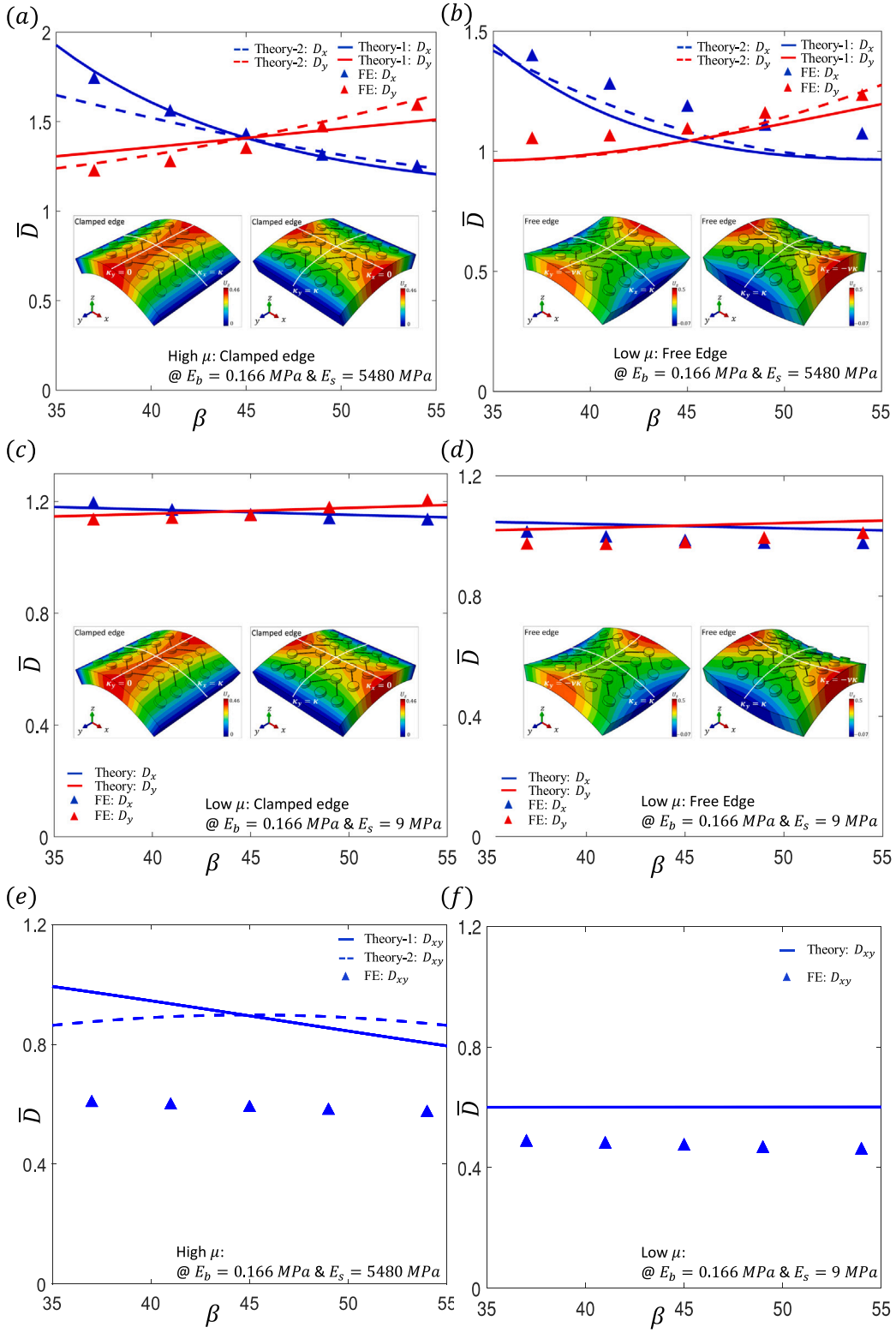

Fig. 5. $\bar{D}$ of architected tendon system for various β with applied curvature in both-directions, and ν of 0.48. (a) and (b) show $\bar{D}$ vs β for μ = (high-μ range - E_s = 5480 and E_b = 0.166 MPa) for clamped and free BC respectively, while (c) and (d) depict $\bar{D}$ vs β for μ = (low-μ range - E_s = 9 and E_b = 0.166 MPa) for clamped and free BC respectively. (e) and (f) depicts the bending rigidity $\bar{D}_{xy}$.

from our model's specific assumptions of string kinematics assuming the substrate Poisson's ratio as our operating Poisson's ratio for plate surface kinematics.

The effective rigidity expressions combine string extension, button inclusion and button rotation effects. This indicates a complex geometry-material interplay distinct from traditional composites. For the stiff tendon (high-μ), the bending rigidity scales as unit cell volume fraction as expected in dilute two-phase composites. However, for relatively soft strings, the bending rigidity does not scale linearly with string volume fraction due to the complex interplay of strings and

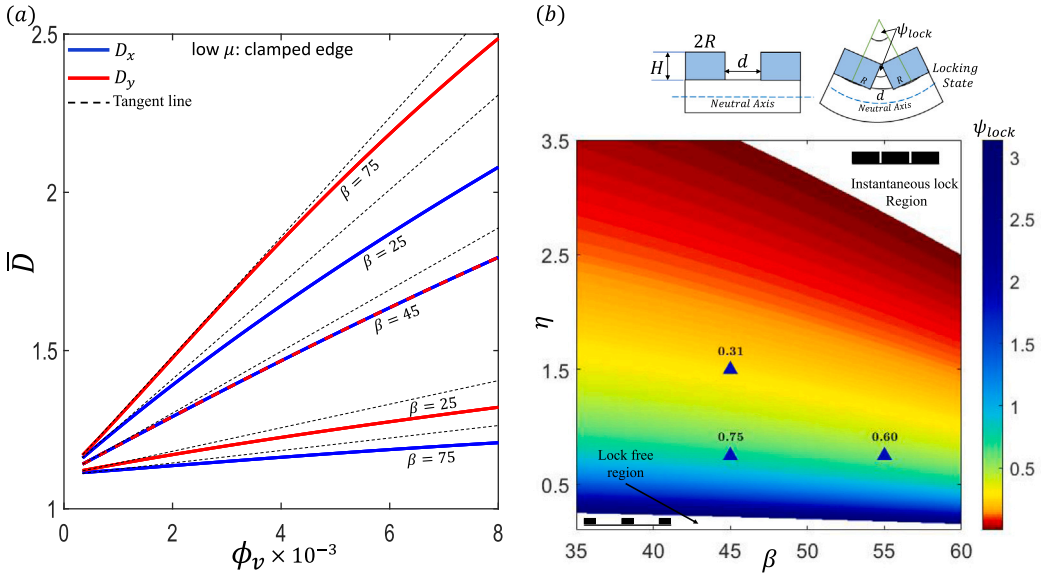

Fig. 6. (a) Theoretical estimation of $\bar{D}$ with ϕ_v at angles of 25°, 45°, and 75° for low-μ and clamped BC with ν of 0.48, (d) (top) schematic unit cell geometry before and after a locking event and (bottom) phase plot of ψ_{lock} with β and η ratios and FE results (blue triangle).

angles (via Γ term in the rigidity expression). This is best explained in Fig. 6(a) where $\bar{D}$ is plotted with string volume fraction. The linear dependence ceases for higher volume fractions and lower angles, unlike traditional woven or particulate composites in dilute limits.

6. Locking behavior

In the concave direction bending, the strings are not engaged but eventually, the buttons would mutually contact leading to a geometrically locked/jammed configuration, Fig. 6(b). To calculate the locking limit, we define $\psi(=\kappa d)$ as substrate bending angle, and d the inner distance between the buttons. From the unit cell depicted in Fig. 6(b) (top), we find $\psi_{lock} = d/H$. Since $d + 2R = 2L_s \cos\beta$, Fig. 4, $\psi_{lock} = \frac{2L_s \cos\beta - 2R}{H}$. This leads to $\psi_{lock} = \frac{2\cos\beta}{\eta} - 2\alpha$ where $\alpha = R/H$. For $\psi_{lock} \geq 0$, $\cos\beta \geq \eta\alpha \implies \cos\beta > \frac{R}{L_s}$. In other word, if $\beta \geq \cos^{-1}\frac{R}{L_s}$ then instantaneous locking occurs in the concave direction. On the contrary, at $\psi >\geq \pi$ or $\eta \leq \frac{cos\beta}{\alpha+\pi/2}$ no locking takes place. These different lock-phases are described using a kinematic lock phase map, Fig. 6(b). As predicted there are three distinct phases of operations spanned by the geometry of the buttons and weave. The phase map also shows that for a given η, locking advances as β increased. This is because increasing β decreases the spacing d. Similarly, for a given weave, higher η advances the locking curvature till at critical η, the phase-boundary of instantaneous locking is achieved. The triangles indicate FE results which are in excellent agreement with analytical expression. Our model also agrees with experiments, Fig. 2 which indicates a sharp rise in stiffness for all weaves as the locking region is reached in the concave bending direction.

7. Conclusion

In conclusion, we derived the architecture-property relationships of a tendon metastructure. The weaves resulted in several broken symmetries leading to a distinct anisotropic structure with nonlinear material-geometry interaction, distinct from traditional woven composites. The structure–property relationships were nonlinear with disproportionate sensitivity towards wound angles for some directions. The analytical models are limited by several factors arising from the boundary conditions, small deformation range, constant Poisson's ratio, string deformation kinematics and high-contrast material combinations. Despite these limitations, our work lays the foundation for a novel metastructure that is capable of creating geometrically tunable material properties. The mathematical model presented in here opens up possibilities for developing programmable metamaterials with adjustable symmetries or spatially varying functionally graded asymmetries which can be tuned in real-time by using actuators such as shape memory alloys, stimuli-responsive coiled spring actuators, and photosensitive polymeric fibers.

CRediT authorship contribution statement

Md Shahjahan Hossain: Writing – original draft, Software, Methodology, Formal analysis, Conceptualization. **Hossein Ebrahimi:** Visualization, Conceptualization. **Ranajay Ghosh:** Writing – review & editing, Supervision, Investigation, Funding acquisition, Conceptualization.

Declaration of competing interest

The authors declare that they have no known competing financial interests or personal relationships that could have appeared to influence the work reported in this paper.

Data availability

Data will be made available on request.

Acknowledgments

This work was supported by the United States National Science Foundation's Civil, Mechanical, and Manufacturing Innovation, CAREER Award #1943886.

Appendix A. Supplementary data

Supplementary material related to this article can be found online at https://doi.org/10.1016/j.jmbbm.2024.106505.

References

Ali, H., Ebrahimi, H., Ghosh, R., 2019. Bending of biomimetic scale covered beams under discrete non-periodic engagement. Int. J. Solids Struct. 166, 22–31.

Amendola, A., Carpentieri, G., De Oliveira, M., Skelton, R., Fraternali, F., 2014. Experimental investigation of the softening–stiffening response of tensegrity prisms under compressive loading. Compos. Struct. 117, 234–243.

Arbabi, A., Arbabi, E., Horie, Y., Kamali, S.M., Faraon, A., 2017. Planar metasurface retroreflector. Nat. Photonics 11 (7), 415–420.

Badawe, M.E., Almoneef, T.S., Ramahi, O.M., 2016. A true metasurface antenna. Sci. Rep. 6 (1), 1–8.

Buehler, M.J., 2006. Nature designs tough collagen: explaining the nanostructure of collagen fibrils. Proc. Natl. Acad. Sci. 103 (33), 12285–12290.

Bundhoo, V., Haslam, E., Birch, B., Park, E.J., 2009. A shape memory alloy-based tendon-driven actuation system for biomimetic artificial fingers, Part I: design and evaluation. Robotica 27 (1), 131–146.

Ebrahimi, H., 2021. Mechanics of low dimensional biomimetic scale metamaterials.

Ebrahimi, H., Ali, H., Ghosh, R., 2020. Coulomb friction in twisting of biomimetic scale-covered substrate. Bioinspiration Biomim. 15 (5), 056013.

Ebrahimi, H., Ali, H., Stephen, J., Ghosh, R., 2021. Fish scales: Primitive basis for modern metamaterials. Europhys. Lett. 133 (6), 68001.

Fish, J., 2003. Multiscale computational engineering. Appl. Math. 2, 17–50.

Ghosh, R., Ebrahimi, H., Vaziri, A., 2014. Contact kinematics of biomimetic scales. Appl. Phys. Lett. 105 (23), 233701.

He, Q., Sun, S., Xiao, S., Zhou, L., 2018. High-efficiency metasurfaces: principles, realizations, and applications. Adv. Opt. Mater. 6 (19), 1800415.

Helfman, G., Collette, B.B., Facey, D.E., Bowen, B.W., 2009. The Diversity of Fishes: Biology, Evolution, and Ecology. John Wiley & Sons.

Hossain, M.S., Ebrahimi, H., Ghosh, R., 2022. Fish scale inspired structures-a review of materials, manufacturing and models. Bioinspiration Biomim..

Jang, J., Song, Y.-U., Ryu, J.-H., 2022. Active-type continuously variable transmission system based on a twisted string actuator. IEEE Robot. Autom. Lett. 7 (2), 2605–2612.

Jeong, U., Kim, K., Kim, S.-H., Choi, H., Youn, B.D., Cho, K.-J., 2021. Reliability analysis of a tendon-driven actuation for soft robots. Int. J. Robot. Res. 40 (1), 494–511.

Jing, X., Mi, H.-Y., Huang, H.-X., Turng, L.-S., 2016. Shape memory thermoplastic polyurethane (TPU)/poly (ε-caprolactone)(PCL) blends as self-knotting sutures. J. Mech. Behav. Biomed. Mater. 64, 94–103.

Knick, C.R., Sharar, D.J., Wilson, A.A., Smith, G.L., Morris, C.J., Bruck, H.A., 2019. High frequency, low power, electrically actuated shape memory alloy MEMS bimorph thermal actuators. J. Micromech. Microeng. 29 (7), 075005.

Lim, S., Luan, H., Zhao, S., Lee, Y., Zhang, Y., Huang, Y., Rogers, J.A., Ahn, J.-H., 2020. Assembly of foldable 3D microstructures using graphene hinges. Adv. Mater. 32 (28), 2001303.

Lu, C., Hsieh, M., Huang, Z., Zhang, C., Lin, Y., Shen, Q., Chen, F., Zhang, L., 2022. Architectural design and additive manufacturing of mechanical metamaterials: A review. Engineering.

Lu, J., Skelton, R.E., 1998. Optimal hybrid control for structures. Comput.-Aided Civ. Infrastruct. Eng. 13 (6), 405–414.

Martini, E., Maci, S., 2014. Metasurface transformation theory. Transform. Electromagn. Metamater.: Fundam. Princ. Appl. 83–116.

Mousanezhad, D., Ebrahimi, H., Haghpanah, B., Ghosh, R., Ajdari, A., Hamouda, A., Vaziri, A., 2015. Spiderweb honeycombs. Int. J. Solids Struct. 66, 218–227.

Mousanezhad, D., Haghpanah, B., Ghosh, R., Hamouda, A.M., Nayeb-Hashemi, H., Vaziri, A., 2016. Elastic properties of chiral, anti-chiral, and hierarchical honeycombs: A simple energy-based approach. Theor. Appl. Mech. Lett. 6 (2), 81–96.

Munyensanga, P., El Mabrouk, K., 2023. Elemental and experimental analysis of modified stent's structure under uniaxial compression load. J. Mech. Behav. Biomed. Mater. 143, 105903.

Popov, D., Gaponov, I., Ryu, J.-H., 2013. Bidirectional elbow exoskeleton based on twisted-string actuators. In: 2013 IEEE/RSJ International Conference on Intelligent Robots and Systems. IEEE, pp. 5853–5858.

Pu, W., Wei, F., Yao, L., Xie, S., 2022. A review of humidity-driven actuator: toward high response speed and practical applications. J. Mater. Sci. 57 (26), 12202–12235.

Rodrigue, H., Wang, W., Han, M.-W., Kim, T.J., Ahn, S.-H., 2017. An overview of shape memory alloy-coupled actuators and robots. Soft Robotics 4 (1), 3–15.

Rutherford, S., Demianiuk, R.M., Benamou, J., Beckett, C., Ness, M.G., Déjardin, L.M., 2015. Effect of intramedullary rod diameter on a string of pearls plate-rod construct in mediolateral bending: An in vitro mechanical study. Vet. Surg. 44 (6), 737–743.

Skelton, R.E., Adhikari, R., Pinaud, J.-P., Chan, W., Helton, J., 2001. An introduction to the mechanics of tensegrity structures. In: Proceedings of the 40th IEEE Conference on Decision and Control (Cat. No. 01CH37228), vol. 5, IEEE, pp. 4254–4259.

Skelton, R.E., De Oliveira, M.C., 2009. Tensegrity Systems, vol. 1, Springer.

Souza, S.A., Muehlbauer, P., Janzen, S., Liu, J., Pott, P.P., 2019. Series and parallel actuation array of elastic micro-twisted string actuators. In: IKMT 2019-Innovative Small Drives and Micro-Motor Systems; 12. ETG/GMM-Symposium. VDE, pp. 1–5.

Stig, F., Hallström, S., 2013. Influence of crimp on 3D-woven fibre reinforced composites. Compos. Struct. 95, 114–122.

Tatari, M., Ebrahimi, H., Ghosh, R., Vaziri, A., Nayeb-Hashemi, H., 2023. Bending stiffness tunability of biomimetic scale covered surfaces via scales orientations. Int. J. Solids Struct. 280, 112406.

Tavakoli, M., Batista, R., Sgrigna, L., 2015. The UC softhand: Light weight adaptive bionic hand with a compact twisted string actuation system. In: Actuators, vol. 5, (1), MDPI, p. 1.

Timoshenko, S., Woinowsky-Krieger, S., et al., 1959. Theory of Plates and Shells, vol. 2, McGraw-hill New York.

Usman, M., Suthar, B., Seong, H., Hawkes, E., Gaponov, I., Ryu, J.-H., 2017. Passive returning mechanism for twisted string actuators. In: 2017 IEEE International Conference on Robotics and Automation. ICRA, IEEE, pp. 3714–3719.

Wang, W., Xiang, C., Liu, Q., Li, M., Zhong, W., Yan, K., Wang, D., 2018. Natural alginate fiber-based actuator driven by water or moisture for energy harvesting and smart controller applications. J. Mater. Chem. A 6 (45), 22599–22608.

Wegst, U.G., Bai, H., Saiz, E., Tomsia, A.P., Ritchie, R.O., 2015. Bioinspired structural materials. Nat. Mater. 14 (1), 23–36.

Wu, W., Hu, W., Qian, G., Liao, H., Xu, X., Berto, F., 2019. Mechanical design and multifunctional applications of chiral mechanical metamaterials: A review. Mater. Des. 180, 107950.

Yu, X., Zhou, J., Liang, H., Jiang, Z., Wu, L., 2018. Mechanical metamaterials associated with stiffness, rigidity and compressibility: A brief review. Prog. Mater. Sci. 94, 114–173.

Zhang, J., Bombara, D., Fowzer, S., Brennan, C., 2020. Compliant and large-strain twisted string actuators using supercoiled polymers. In: 2020 3rd IEEE International Conference on Soft Robotics. (RoboSoft), IEEE, pp. 201–207.

Zhang, J., Ohsaki, M., 2015. Tensegrity Structures, vol. 7, Springer.